ADVANCED FUNCTIONAL MATERIALS
www.afm-journal.de

Mixed Halide Formation in Lead-Free Antimony-Based Halide Perovskite for Boosted CO_2 Photoreduction: Beyond Band Gap Tuning

*Jiale Lee, Wei-Kean Chong, Steven Hao Wan Kok, Boon-Junn Ng, Xin Ying Kong, Siang-Piao Chai, and Lling-Lling Tan**

Photocatalytic conversion of carbon dioxide (CO_2) into value-added fuels is a vastly promising anthropogenic chemical carbon cycle to combat the greenhouse effect while meeting the ever-increasing energy demand. Recently, lead-based halide perovskites have demonstrated great potential in various applications including photochemical reduction of CO_2. However, in view of lead toxicity, the exploration of a lead-free alternative is crucial for long term application. Herein, a series of lead-free mixed halide perovskites $Cs_3Sb_2Cl_xBr_{9-x}$ ($0 \leq x \leq 9$) is prepared via a facile antisolvent recrystallization technique, where the incorporation of a secondary halide enhances the charge transfer and separation while allowing precise tuning of bandgap between 2.59 and 2.90 eV. Theoretical calculations further reveal that the formation of mixed Cl/Br halides engenders favorable charge redistribution due to lower octahedral distortion, which in turn strengthens CO_2 adsorption and activation. Under visible light illumination, the optimal dual halide perovskite, $Cs_3Sb_2Cl_4Br_5$ manifests substantial twofold and fourfold enhancements of CH_4 yield over the single halide perovskite, $Cs_3Sb_2Br_9$ and $Cs_3Sb_2Cl_9$, respectively. In brief, this study provides a compelling demonstration of lead-free mixed halide perovskites for photocatalytic CO_2 reduction, and it is anticipated to drive further application of perovskite-based photocatalysts toward a diverse range of artificial photoredox reactions.

1. Introduction

Meeting the ever-increasing energy demand from expeditious industrialization and population growth worldwide is one of the highly pressing global issues. As a matter of fact, this surging energy requirement has been, thus far, primarily met by the large-scale exhaustion of finite fossil fuels, leading to massive anthropogenic carbon dioxide (CO_2) emission.[1] As of December 2022, the concentration of CO_2 in our atmosphere has reached 418.82 ppm,[2] which is about 1.5 times higher than that of the pre-industrial revolution level.[3] Accompanied by the hastening depletion of fossil fuels, this phenomenon has led to deleterious effects on our environment in the form of global warming, melting glaciers, rising sea level, climate change, land degradation and desertification.[4] Therefore, there is an urgency to curb greenhouse gas emissions and yet continue to meet the energy necessary for a rising global population in a sustainable manner. Countermeasures, CO_2 capture, utilization, and storage (CCUS) are regarded as a promising strategy for meeting CO_2 emission reduction targets.[5] Alternatively, the concept of converting CO_2 into synthetic fuels offers an intriguing solution toward building a sustainable circular carbon economy. In this context, artificial photocatalysis, which involves the photocatalytic reduction of CO_2 into valuable carbon-neutral fuels using solar energy is regarded as a promising approach to simultaneously address the imminent energy scarcity and alleviate greenhouse gas emissions.[6] The chemical transformation of CO_2 into CH_4 via mild photocatalytic reaction aligns with the principles of sustainable energy development and green synthesis, signifying its pivotal importance from fundamental research to real-world applications for carbon reduction. In spite of the numerous benefits, chemical CO_2 conversion is challenging given that multiple reaction steps are involved due to the thermodynamic stability of CO_2 molecule.[7] Consequently, the efficiency of light-driven CO_2 reduction is still far from meeting large-scale industrial applications. Nevertheless, in the past several decades, prevalent efforts have been devoted in this research endeavor, and thus far, the activity of photocatalytic CO_2 reduction has made substantial advancement.[8]

J. Lee, W.-K. Chong, S. H. W. Kok, B.-J. Ng, S.-P. Chai, L.-L. Tan
Multidisciplinary Platform of Advanced Engineering
Department of Chemical Engineering
School of Engineering
Monash University Malaysia
Jalan Lagoon Selatan, Bandar Sunway, Selangor 47500, Malaysia
E-mail: tan.llinglling@monash.edu

X. Y. Kong
School of Chemistry, Chemical Engineering and Biotechnology
Nanyang Technological University, Singapore
21 Nanyang Link, Singapore 637371, Singapore

The ORCID identification number(s) for the author(s) of this article can be found under https://doi.org/10.1002/adfm.202303430

DOI: 10.1002/adfm.202303430

Recently, metal halide perovskites have been extensively studied as photocatalyst due to their outstanding light harvesting capability, tuneable band structure, exceptional charge transfer dynamics and flexible crystal structure, rendering them as ideal photocatalysts for CO_2 reduction reactions.[9] Especially, lead halide perovskites (LHPs), a common class of metal halide, have attracted vast attention in the past several years with significant progress achieved for CO_2 conversion.[10] Nonetheless, the inherent lead toxicity, environmental pollution and health concerns associated with the usage of LHPs greatly restrict their practical applications.[11] Hence, extensive efforts have been devoted to the construction of lead-free halides perovskite in the pursuit of green and sustainable material development. Specifically, these efforts focus on lead replacement with more environmentally benign metal centres while retaining the excellent photo-physical and optoelectrical properties of halide perovskite.[12] In this regard, the development of lead-free halide perovskites by substituting Pb^{2+} in the perovskite structure with less toxic metal centres such as the divalent lone-pair metal cations (Sn^{2+}, Ge^{2+}) and trivalent lone-pair cations (Bi^{3+}, Sb^{3+}) have been studied for integration into the wide optoelectronic field such as solar cell devices, photodetectors, and light emitting diodes.[13] Among the lead-free halide perovskites, the antimony -based halide perovskites for photocatalytic CO_2 reduction to CH_4 have scarcely been reported. Xu et al. and Tang et al. reported the high efficiency photoreduction of CO_2 to CO using the lead-free $Cs_3Sb_2I_9$ photocatalyst while Geyer et al. synthesized pure and uniform $Cs_3Sb_2Br_9$ nanocrystals for enhanced CO yield.[14] Meanwhile, Tang et al. synthesized $Cs_3Sb_2(Br_xI_{1-x})_9$ ($0 \leq x \leq 1$) mixed halide perovskite nanoplatelets for photocatalytic CO_2 reduction to CO via ligand-assisted reprecipitation technique.[15] However, the fabrication methods adopted were dependent on high temperature and/or required an inert atmosphere.

In this work, all-inorganic caesium antimony mixed halide perovskites $Cs_3Sb_2Cl_xBr_{9-x}$ are designed and explored for visible light-driven CO_2 reduction to CH_4 for the first time. To the best of our knowledge, no prior work pertinent to the antimony-based mixed halide perovskite, precisely on the $Cs_3Sb_2Cl_xBr_{9-x}$ ($0 \leq x \leq 9$) for photocatalytic CO_2 reduction has been reported. Unlike the commonly adopted synthesis method, our study presents a room temperature and ligand-free fabrication route for the mixed halide perovskites. In addition to material development and application for photocatalytic reactions, this study aims to shed light on the fundamental aspects involving material properties and the effects associated to compositional manipulation on halide perovskite via experimental and computational findings. Although the X-site halide-anion regulation is a widely adopted strategy for performance and stability enhancement in LHPs, the specific impact on active sites upon mixed halides formation in antimony-based perovskite photocatalyst has yet to be revealed.[16] Essentially, the introduction of a secondary halide induces favorable charge redistribution and leads to superior CO_2 adsorption and activation on the surface halogen-associated active sites as revealed by first-principle calculations. Under a 6-h visible light irradiation, the optimal sample $Cs_3Sb_2Cl_4Br_5$ (CAHP–4) exhibits a twofold and fourfold enhancement in CO_2 photoreduction to CH_4 relative to its single halide perovskite counterparts, $Cs_3Sb_2Br_9$(CAHP-0) and $Cs_3Sb_2Cl_9$ (CAHP-9), respectively. Experimental characterization further unravels the contributing factors to the ameliorated photoactivity including promoted charge transfer and suppressed charge recombination. This study demonstrates that the direct tuning of halide compositions in $Cs_3Sb_2Cl_xBr_{9-x}$ is feasible and efficacious to precisely control the optical property, strengthening CO_2 adsorption and activation as well as enhancing the charge transfer and separation efficiencies. All in all, this work presents an effective and environmentally friendly approach for material development and performance enhancement toward photocatalytic CO_2 reduction as part of the unceasing efforts in pivoting toward a more sustainable and thriving future.

2. Results and Discussion

2.1. Synthesis and Characterization of Caesium Antimony Halide Perovskites

The antimony–based perovskite photocatalyst were synthesized via a facile and ligand-free anti-solvent recrystallization method at ambient conditions, where dimethyl sulfoxide (DMSO) was used for the dissolution of caesium and antimony halides while isopropanol (IPA) was applied as the antisolvent. The caesium antimony halide perovskites $Cs_3Sb_2Cl_xBr_{9-x}$ ($0 \leq x \leq 9$) were labeled as CAHP-*x*, where $x = 0$, 2, 4, 6, and 9 for $Cs_3Sb_2Br_9$, $Cs_3Sb_2Cl_2Br_7$, $Cs_3Sb_2Cl_4Br_5$, $Cs_3Sb_2Cl_6Br_3$, and $Cs_3Sb_2Cl_9$, respectively. Powder X–ray diffraction (PXRD) measurements (**Figure 1**a) were executed to study the crystal structures of CAHP-*x* with varying Cl/Br compositions. The XRD patterns reveal that all samples are crystallized in the trigonal space group, $P\bar{3}m1$ (164). The diffraction peaks of CAHP-0 and CAHP-9 are well-indexed to the standard $Cs_3Sb_2Br_9$ (JCPDS, no. 77–1055) and $Cs_3Sb_2Cl_9$ (JCPDS, no. 73–0305), respectively. The prominent peaks of CAHP-0 at 22.34°, 27.47°, 31.88°, and 45.72° correspond to the (012), (201), (022), and (024) characteristic crystal face of $Cs_3Sb_2Br_9$. Meanwhile, the major peaks of CAHP-9 at 23.35°, 28.66°, 33.30°, 41.03°, 47.81° are attributed to the (102), (003), (022), (014), and (204) crystal plane of $Cs_3Sb_2Cl_9$ perovskite structure. For CAHP-9, the impurity peaks at 30.62° and 43.87° (denoted with *) are most likely assigned to the unreacted CsCl due to the its low solubility in conventional solvents such as DMSO and dimethyl formamide (DMF).[17] As observed from the XRD patterns, all the diffraction peaks are monotonically shifted to a lower angle as the halide sites are varied from pure Cl (CAHP-9), to mixed Cl/Br (CAHP-6, CAHP-4, CAHP-2), and to pure Br (CAHP-0). As the value of *x* decreases, the most intense peak which corresponds to the (022) plane is left-shifted from 33.32°, 32.79°, 32.50°, 32.12°, to 31.86° due to the replacement of Cl ions by Br ions with a larger ionic radius ($Cl^- = 1.81$ Å; $Br^- = 1.96$ Å). This suggests that the as-synthesized CAHP–x_{xx} samples (CAHP-2, CAHP-4, and CAHP-6) are solid solutions rather than mixtures of $Cs_3Sb_2Cl_9$ and $Cs_3Sb_2Br_9$, as the characteristic peaks of the mixed halides fall between the pure-phase positions. Furthermore, the expansion in the calculated lattice parameters *a*, *c*, and unit cell volume from XRD analysis (Table S1, Supporting Information) further validates the incorporation of Br into the $Cs_3Sb_2Cl_9$ lattice. Notably, the experimental lattice parameters and cell volume exhibited a linear relationship with the increasing replacement of Br by Cl, where no significant deviation ($R^2 \geq 0.9978$) from the Vegard's law is noted as depicted

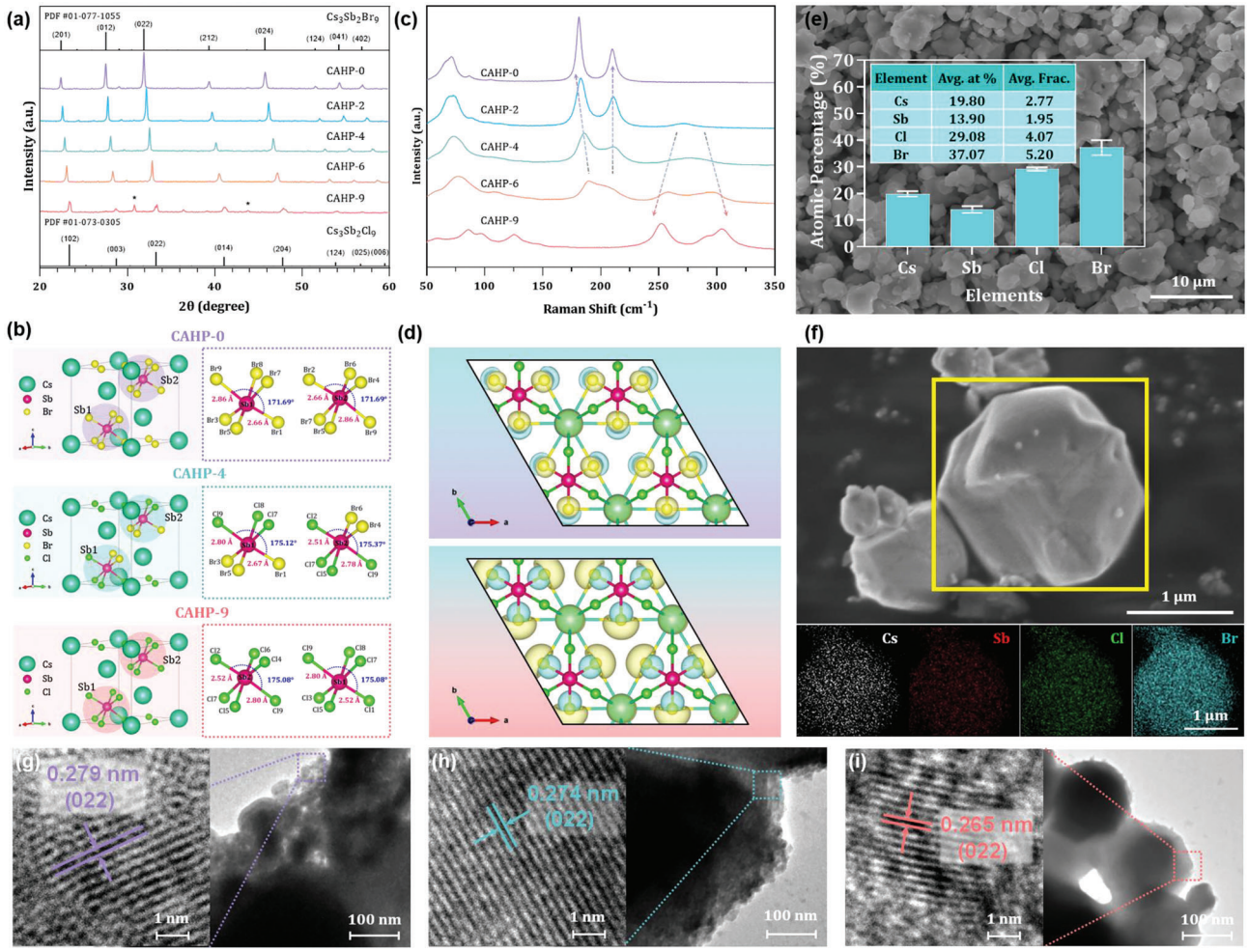

Figure 1. a) XRD pattern of the CAHP-*x* powders. b) Crystal structure of CAHP-0, CAHP-4 and CAHP-9; the left structure shows the representative 1 × 1 unit cell and the right is the SbX_6 octahedra. CAHP-4 of the most favorable Cl and Br positions is obtained from the configuration with the lowest formation energy. c) Raman spectra of CAHP-*x*. d) 3D charge density difference (isosurface level, 0.008 e $Å^{-3}$) for CAHP-4 relative to CAHP-0 (top) and CAHP-4 relative to CAHP-9 (bottom). The yellow and cyan regions denote positive and negative electron density isosurface, respectively. e) FESEM and EDX analysis (inset) of CAHP-4. f) FESEM image and the corresponding EDX-mapping of Cs, Sb, Cl, and Br elements on CAHP-4. TEM and HRTEM (inset) of g) CAHP-0, h) CAHP-4, and i) CAHP-9.

in Figure S2a,b, Supporting Information.[18] This reinforces the successful insertion of Br into the crystal lattice of the halide perovskite, with a similar overall lattice arrangement.

Microstructure analysis is conducive in comprehending the resulting alterations due to replacement of Cl atoms by Br atoms. As portrayed in Figure 1b, $Cs_3Sb_2X_9$ presents a structure comprising of corner-sharing SbX_6 octahedra. Upon five Br atoms substitution (CAHP-4), the difference in bond lengths ($\Delta\ell$) relative to CAHP-9 and CAHP-0 noticeably decreased (Table S2, Supporting Information). This in turn diminishes the magnitude of octahedral distortion (δ) as summarized in Table S3, Supporting Information. Attributing to the difference in electronegativity of the anions, the Sb–X (bridging anion) bonds are compressed while the Sb–X (terminal anion) bonds are elongated in the structure of CAHP-4 (Table S2, Supporting Information). Since the Br atoms tend to occupy the terminal positions, the terminal Sb–X bonds lengthen due to the weaker electronegativity of Br atoms. As a result, the strongly localized charges are redistributed and subsequently impacts the photoelectric and surface catalytic properties of the semiconductors.[19] (Refer to Figure S10, Supporting Information to identify the terminal and bridging positions in the CAHP-*x* structure). This charge redistribution phenomenon is apparent from Figure 1d, where the electron accumulation and depletion regions are portrayed in yellow and cyan, respectively. As reflected from the charge density difference of CAHP-4 relative to CAHP-0 (Figure 1d, top) and CAHP-9 (Figure 1d, bottom), there is a significant charge redistribution across the whole framework after the introduction of a secondary halide, which could provide more charge carriers for the enhancement of photocatalytic reactions.[20] Conspicuously, the charge density difference between CAHP-4 and CAHP-9 is denser than that of CAHP-4 and CAHP-0, suggesting that the enhancement effect of mixed halide formation toward CAHP-9 would be greater than that of CAHP-0. This was proven through the CO_2 photoreduction experiment, which would be elucidated in the later section. It is noteworthy that the magnitude of charge

redistribution is closely associated to the octahedral distortion as an identical trend is observed on the charge density difference and the variance in octahedral distortion (Δd), whereby a greater Δd leads to a more prominent charge redistribution.

A more in-depth understanding of microstructure alteration can be studied from Raman characterization. As illustrated in Figure 1c, the single halide samples CAHP-0 and CAHP-9 display two distinct Raman bands in the region of 150–350 cm^{-1} while an additional band is spotted for the mixed halides samples of CAHP-2, CAHP-4, and CAHP-6. Correspondingly, Raman shifts at 181.34 and 209.65 cm^{-1} are identified for CAHP-0 while CAHP-9 show bands at higher frequencies of 252.46 and 304.11 cm^{-1}.[21] These peaks are assigned to the stretching vibrations of the stronger terminal Sb–X bonds in SbX_6 octahedra.[20a] For the mixed halide perovskites, the vibration information assigned to both Sb–Br and Sb–Cl bonds are evident from the three peaks observed within the same region (150–350 cm^{-1}) of the Raman spectra. As the ratio of Cl: Br increases, the two peaks due to the stretching of Sb–Br shifted slightly to a higher frequency with reduced intensities and coalesced into a single peak for when the Cl: Br ratio is at 6:3 (CAHP-6). Vice versa, the new Sb–Cl peak at ≈273.5 cm^{-1} intensifies and gradually splits into two peaks as Cl: Br rises, implying that Sb–Cl bonds are present in the microstructure with $SbBr_6$ and $SbCl_6$ octahedra mixed and distributed throughout the structure. In addition to these identifiable bands, the broader bands at the region of lower frequency (50–150 cm^{-1}) are also present, attributing to the movement of Br or Cl atoms without the involvement of the Sb atom.[22] One of these Raman bands corresponds to the vibration of octahedra along the x- and y-axes, while the other two may result from the deformational vibration of the octahedra.[21] The field emission scanning electron microscopy (FESEM) images of CAHP-*x* (Figure 1e, Figure S3a–e, Supporting Information) show that the samples have irregular morphologies with varying sizes. As disclosed by the FESEM-energy dispersive X–ray (EDX) mapping images in Figure 1f and Figures S4–S8, Supporting Information, CAHP-*x* are confirmed to be composed of Cs, Sb, and halogen elements (Br and/or Cl), with a uniform distribution. The elemental composition as summarized in the inset of Figure 1e and Figures S4–S8, Supporting Information, also confirm the stoichiometric ratio of the halide perovskite $Cs_3Sb_2X_9$ (X = halide) in the CAHP-*x* samples. The high-resolution transmission electron miscroscopy (HRTEM) image depicted in the inset of Figure 1g–i show the good crystalline and clear lattice fringes of CAHP-0, CAHP-4, and CAHP-9. The lattice fringes of CAHP-0 and CAHP-9 demonstrated spacing of 0.279 and 0.265 nm, respectively. Moreover, the interplanar lattice spacing of CAHP-4 at 0.274 nm falls between those of pure $Cs_3Sb_2Br_9$ and $Cs_3Sb_2Cl_9$, further confirming the successful formation of solid solution containing mixed halides.

X–ray photoelectron spectroscopy (XPS) analysis was carried out to examine variances in both chemical environment and charge distributions of $Cs_3Sb_2Br_9$ (CAHP-0), $Cs_3Sb_2Cl_4Br_5$ (CAHP-4), and $Cs_3Sb_2Cl_9$ (CAHP-9). The survey spectra as shown in Figure S22, Supporting Information, confirm that the as-synthesized samples are composed of Cs, Sb, and halogen elements (Cl and/or Br), without any other impurities. The presence of mixed halides comprising both Cl and Br in CAHP-4 is also evident from the survey scan as highlighted in yellow and green. Besides, the XPS elemental composition (Table S4, Supporting Information) of CAHP-0, CAHP-4, and CAHP-9 are identical to the EDX analysis results, further validating the presence of Cs, Sb, Cl, and/or Br following the expression of $Cs_3Sb_2X_9$. As depicted in **Figure 2**a,b, a slight negative shift in binding energies of Cs 3d and Sb 3d were observed from CAHP-0 to CAHP-9, implying denser electrons in the vicinity of Cs and Sb due the lower electronegativity of Br than that of Cl. The reduced binding energies of Cs 3d and Sb 3d in CAHP-4 is also likely to be contributed by the weakened internal octahedra distortion, inducing dispersed electronic distributions.[19a,20a] Conversely, the binding energy of Br 3d is blue shifted from 69.4 and 68.4 eV of CAHP-0 to 70.0 and 69.0 eV of CAHP-4 (Figure 2c), illustrating the strengthening interaction between Sb and Br after the incorporation of Cl to form mixed halides. Likewise, the same phenomenon is encountered in the comparison of Cl 2p binding energies between CAHP-9 and CAHP-4 (Figure 2d). The higher binding energies of Cl and Br in the mixed halide perovskite are likely contributed by electron density redistribution and change in bonding environment. This phenomenon of an overall increased binding energy of halogens in mixed halides relative to their pure halide counterparts has also been observed in other reported works.[23] Overall, the XPS results indicate that the bonding context of Cs, Sb, and halide atoms is altered due to the co-existence of Br and Cl.

2.2. Study of Optoelectronic Properties

Based on reported studies, the trigonal $Cs_3Sb_2Br_9$ has a direct band gap (E_g) while trigonal $Cs_3Sb_2Cl_9$ has an indirect E_g.[24] To estimate the E_g of the as-synthesized samples, the Tauc plot of the Kubelka–Munk (KM) function $[F(R) \cdot h\nu]^2$ versus hν and $[F(R) \cdot h\nu]^{1/2}$ versus hν can be applied for semiconductors of direct and indirect E_g, respectively. However, the E_g type of the mixed halide perovskites is uncertain. To investigate the alteration of electronic properties due to varying halide composition, the projected density of states (DOS) and band structure calculations were performed on the lowest formation energy (E_{form}) structures of CAHP-0, CAHP-2, CAHP-4, CAHP-6, and CAHP-9 obtained previously. As observed from **Figure 3**a (left), CAHP-0 possess a direct E_g of 1.64 eV with valence band maximum (VBM) and conduction band minimum (CBM) at the Γ point. As illustrated in the DOS plot of CAHP-0 in Figure 3a (right), the VB is largely consisting of filled Br 4p states while the CB is attributed to the mixed Sb 5p and Br 4p orbitals. Meanwhile, the Cs s states neither contribute to the VB nor the CB. With the introduction of Cl into the caesium antimony halide perovskite, the E_g enlarges with increasing Cl content (Figure 3b and Figure S23a,b, Supporting Information) due to the low-lying valence p-orbitals of Cl relative to Br as depicted in the DOS of CAHP-2, CAHP-4, and CAHP-6. This is compatible with the blue shift of absorption edge from CAHP-0 to CAHP-9 (Figure 3d), implying the widening of E_g. Analogously, the VB of the mixed halide perovskites mainly consist of Br 4p orbitals but with the addition of Cl 3p orbitals while the CB contains mixed Sb 5p, Br 4p, and Cl 3p states. Referring to the band structure diagrams shown in Figure 3b and Figure S23a,b, Supporting Information, CAHP-2, CAHP-4, and CAHP-6 retain the nature of direct E_g with both VBM and CBM

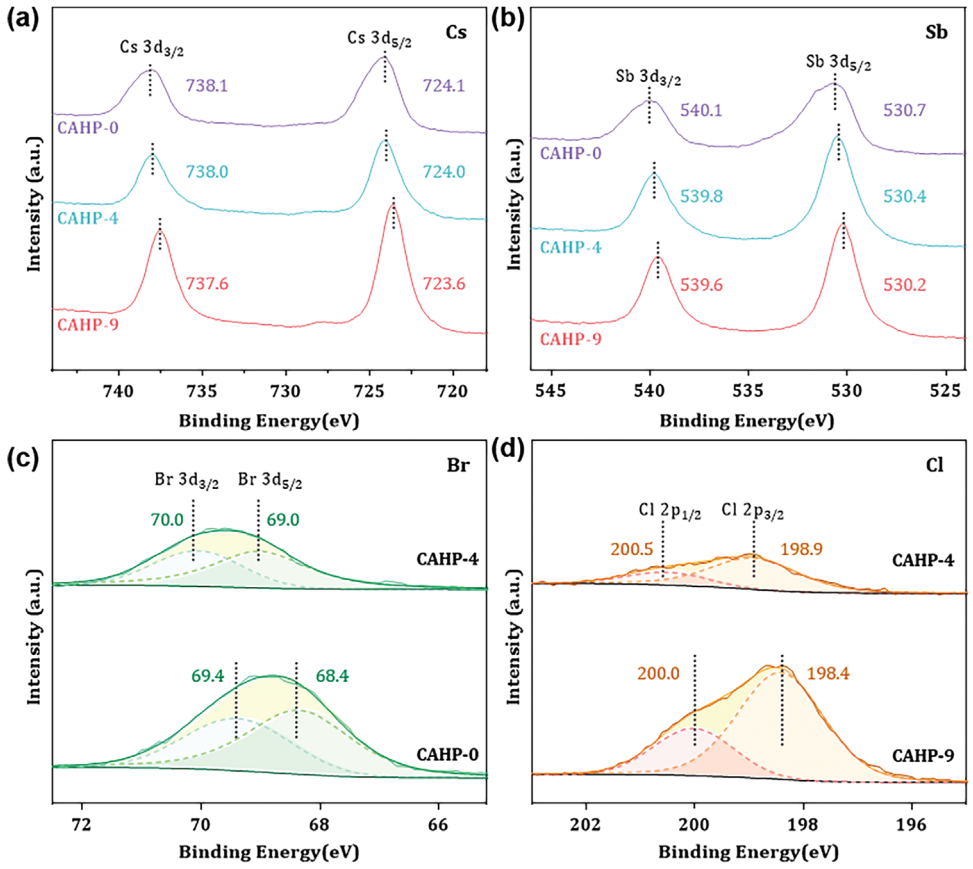

Figure 2. XPS narrow scan of a) Cs 3d, b) Sb 3d, c) Br 3d, and d) Cl 2p of CAHP-0, CAHP-4, and CAHP-9.

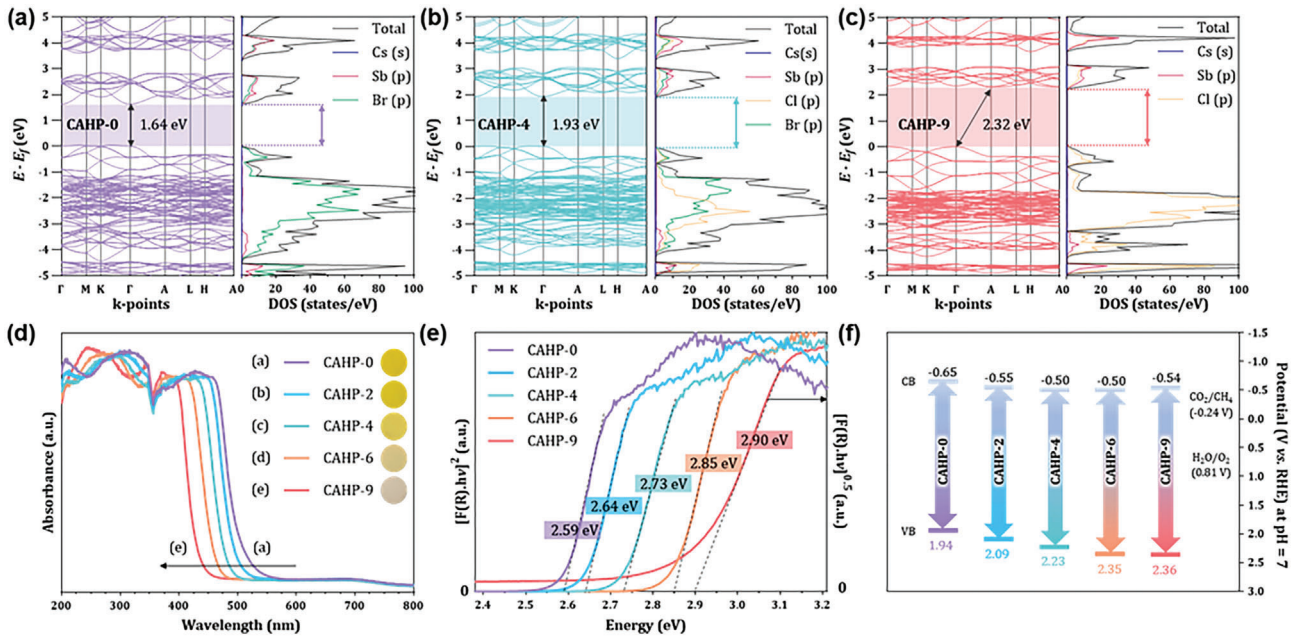

Figure 3. Calculated band structure (left), TDOS and PDOS (right) of a) CAHP-0, b) CAHP-2, c) CAHP-4, d) UV–vis DRS and photos (inset) of CAHP-*x*. e) Tauc plot of the KM function of CAHP-*x*, where all the data is plotted on the left y-axis ($[F(R)\cdot h\nu]^2$ versus $h\nu$) except CAHP-9. f) Band structure of CAHP-*x*.

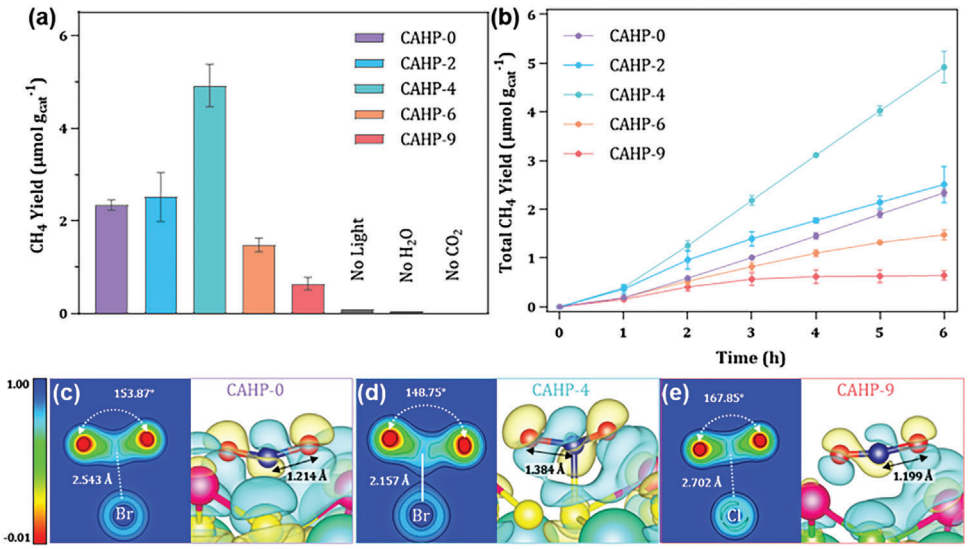

Figure 4. a) Cumulative CH_4 yield in 6 h and b) time-yield plots of CH_4 generation over CAHP-*x* under visible light irradiation. The electron localization function (ELF) (left) of CO_2 molecules on the X5 active sites and charge difference distributions (right) of c) CAHP-0, d) CAHP-4, and e) CAHP-9 after CO_2 adsorption (charge accumulation is denoted in yellow and depletion in cyan).

located at the Γ point. As for CAHP-9 (Figure 3c), an indirect E_g of 2.32 eV is computed, with VBM at the Γ point and CBM at the *A* point. As presented in Figure 3d, an obvious red-shift is observed as the amount of Br atoms increases from CAHP-9 to CAHP-0. The band structures of $Cs_3Sb_2Cl_7Br_2$ (CAHP-7) and $Cs_3Sb_2Cl_8Br_1$ (CAHP-8) were also computed to determine the point at which the indirect E_g transforms to a direct E_g as displayed in Figure S24, Supporting Information. Interestingly, the indirect E_g nature remains when one Br atom is present and transformed into a direct E_g upon two Br atoms substitution. In accordance with the outcome of computational calculations, the optical E_g of CAHP-0, CAHP-2, CAHP-4, and CAHP-6 were evaluated with the KM equation for direct E_g while the KM function for indirect E_g was applied on CAHP-9 (Figure 3e). The band gaps are experimentally obtained to be 2.59, 2.64, 2.73, 2.84, and 2.90 eV for CAHP-0, CAHP-2, CAHP-4, CAHP-6, and CAHP-9, respectively. The experimental E_g is larger than the calculated E_g as expected due to the general underestimation by density functional theory (DFT) calculation.[25] Nonetheless, the DOS calculation certifies that E_g widens from CAHP-0 to CAHP-9 albeit rather underestimated, which is well consistent with the experimental results.

To investigate the nature of semiconductor and flat band potential (E_{fb}) of CAHP-*x*, the Mott–Schottky (MS) plots were constructed based on electrochemical measurements as depicted in Figure S25a–e, Supporting Information. Based on the MS plots, all the samples exhibit *n*-type behavior corresponding to the positive slopes, with their CB edges estimated to be −0.65, −0.55, −0.50, −0.50 and −0.54 versus NHE at pH = 7 for CAHP-0, CAHP-2, CAHP-4, CAHP-6, and CAHP-9, respectively, as detailed in the Supplementary Information (Section 8). The corresponding VB potentials were determined using the following equation:

$$E_{VB} = E_{CB} + E_g \quad (1)$$

The calculated band structures are displayed in Figure 3f. All the CAHP-*x* samples possess suitable E_g as well as appropriate band edge positions to realized CO_2 photoreduction to CH_4. As expected, the VB edges are shifted downward as the substitution of Cl increases, which is well aligned with the theoretical calculations.

2.3. Photocatalytic CO_2 Reduction and the Underlying Mechanism

The photocatalytic performance of the CAHP-*x* samples for CO_2 reduction to CH_4 were explored in a gas-solid interface, with injected humidified CO_2 and visible light illumination. A series of control experiments were carried out under i) dark condition (no light), ii) dry CO_2 flow (no H_2O), and iii) a mixture of N_2/H_2O flow (no CO_2). Under all these experimental conditions, negligible to no hydrocarbon products were detected, implying that the CH_4 is indeed generated solely from the photocatalytic CO_2 reduction reaction, thereby excluding the possibilities of carbon residual decomposition and self-photolysis. As displayed in **Figure 4**a,b, CAHP-4 exhibits the highest photoreduction activity with 4.92 μmol g^{-1} of CH_4 yield after 6 h of visible light irradiation, which is approximately twofold and fourfold higher than that of single halide perovskite CAHP-0 and CAHP-9, respectively. This suggests that the regulation of mixed halogen is an effective approach in boosting photocatalytic CO_2 reduction activity. A similar trend was also observed when the samples are subjected to full spectrum light irradiation for CO_2 reduction (Figure S29, Supporting Information), attesting CAHP-4 as the best-performing photocatalyst among the halide perovskites of various Cl/Br compositions. As compared to the lead-free perovskite-based photocatalysts reported thus far (Table S5, Supporting Information), $Cs_3Sb_2Cl_4Br_5$ shows comparable performance of light-driven CO_2 reduction to CH_4 in a gas-solid

system. Although this small-scale laboratory production has yet to realize meaningful levels of CH_4 generation for practical applications, the fundamental studies and research output could serve as valuable stepping stones toward efficient photocatalytic chemical transformation. To propel photocatalytic systems a step closer to sustainability, practical applications and commercial success, the stability, durability, and recyclability features are indispensable. As such, the thermal and photoactivity stabilities of CAHP-4 were validated through thermogravimetric analysis (TGA) and CO_2 reduction cyclic tests as depicted in Figures S26 and S31, Supporting Information. There was also no significant deviation on the XRD and Raman patterns (Figure S32a,b, Supporting Information) before and after 3 runs of photocatalytic reactions, indicating the excellent structural and chemical stabilities of CAHP-4.

As the adsorption and activation of CO_2 holds an important role in the process of CO_2 reduction, DFT calculations were further performed to examine the essential differences between the mixed halide perovskite (CAHP-4) and single halide perovskites (CAHP-0 and CAHP-9). All the possible adsorption models acquired from the DFT structure optimization toward CO_2 on the various atoms of the perovskites are presented in Figure S27, Supporting Information. Based on the results, physisorption occurs in all the listed CO_2 adsorption configurations, except for the case where CO_2 exhibited chemisorption on Br5 atom of CAHP-4. Upon adsorption on Br5 of CAHP-4 (Figure 4d), the CO_2 moiety shows a bent configuration with an O=C=O angle of 148.75° while the C–O bonds of CO_2 are elongated from 1.163 to 1.384 Å, revealing the weakening of C–O bond. This remarkably suggests the strong chemisorption and activation of CO_2 by CAHP-4. Generally, the CO_2 molecule becomes electrophilic when it is bent from its linear equilibrium geometry, as this lowers the energy level of the lowest unoccupied molecular orbital (LUMO).[26] Thus, the greater extend of bending promotes electron transfer to CO_2, which forms a CO_2 radical anion of high reactivity with the catalyst. Under the same configuration, CO_2 showed physical adsorption on X5 (X = Br or Cl) of CAHP-0 and CAHP-9 instead, with a further distance between CO_2 and both CAHP-0 and CAHP-9 as demonstrated in the electron localization function (ELF) image (Figure 4c,e, left). This reveals that CO_2 is better adsorbed and more easily activated on the identical X5 site of CAHP-4. The differences in CO_2 activation between CAHP-4 and the single halide perovskites were further assessed based on visualization of the microelectronic interactions between CO_2 molecules and the catalyst surface, which are represented as charge difference distribution images in Figure 4c–e (right). Denser electrons are accumulated around the CO_2 and efficacious electron transfer from X5 to CO_2 is evident in CAHP-4 while weaker electron transfer is observed for CAHP-0 and CAHP-9. It is also worth noting that the same trend is reflected in the other configurations (Figure S28, Supporting Information), where CO_2 adsorption on X1, X3, and X5 of CAHP-4 is clearly stronger than that of CAHP-0 and CAHP-9. Therefore, the presence of mixed halides could potentially alter the charge distribution and improve the force between CO_2 and the active sites as demonstrated by CAHP-4.

In addition to CO_2 adsorption, the charge transport and separation behavior crucial in redox reactions are also investigated to unveil the basis of enhancement in CO_2 reduction performance. Photoelectrochemical experiments were conducted to probe the charge transfer and separation dynamics of the samples. As depicted in **Figure 5**a, all the samples show photocurrent response at 0 V versus Ag/AgCl as recorded through on-off cycles of intermittent light irradiation, manifesting that the as-synthesized samples can be excited to generate electrons. A negative current is detected when the light hits the surface of the samples, inferring that reduction reactions take part on the electrode surface.[27] Generally, a stronger photocurrent intensity corresponds to a higher charge transfer and separation efficiency.[28] Among the CAHP-x samples, CAHP-4 demonstrated the highest current density, which strongly indicates its excellent charge mobility, separation, and recombination inhibition. This is further validated with the distinctly diminished semicircle of the Nyquist plot as illustrated in Figure 5b, which postulates an ultra-low charge transfer resistance with accelerated charge separation and transfer process. The phenomenon of promoted charge carrier transport and separation attributed to halide regulation has also been reported in several works.[29] Furthermore, the behavior of photoexcited electron-hole pairs was also investigated by Raman photoluminescence (PL) analysis to gain insights on the charge recombination rate within the photocatalyst over a wavelength range. As observed from Figure 5c, PL emission range of the CAHP-x samples from $x = 9$ to 0 were red-shifted. This is anticipated for the modulation of band structure as halogen sites were varied from pure Cl to mixed Cl and Br to pure Br. By comparing the PL peak intensities, it is inferred that CAHP-9 demonstrated the highest charge recombination probability, while CAHP-4 exhibits the most efficient recombination quenching. In addition, the time-resolved PL spectra were measured to probe the charge transfer dynamics as shown in Figure S30 and Table S6, Supporting Information. The fluorescence decay curves of the CAHP-x samples were fitted to a standard bi-exponent function of $I(t) = A_1 \exp\frac{-t}{\tau_1} + A_2 \exp\frac{-t}{\tau_2}$, where A and t denote the relative component amplitude and lifetime, respectively.[30] According to the fitted values, CAHP-4 demonstrated the longest average lifetimes (τ_{ave}) of 0.61 ns, inferring that CAHP-4 could potentially offer more free charges to facilitate surface redox reactions.[31] Credibly, these findings have collectively corroborated that CAHP-4 exhibits a quicker transfer and separation of photogenerated charge carriers along with a lower charge recombination rate, which are highly beneficial for effective photocatalytic CO_2 reduction.

By incorporating the experimental characterization and computational results above, a reasonable elucidation of the CO_2 photoreduction to CH_4 over CAHP-4 is illustrated in **Figure 6**. First, the CO_2 and H_2O molecules are adsorbed on the surface of CAHP-4. Under visible light irradiation with energy equal to or greater than the E_g, electron-hole pairs are created in which the electrons are excited to the CB while holes retain in the VB of CAHP-4. At the VB, the adsorbed H_2O molecules are oxidized by photoinduced holes to form H^+ and O_2. Simultaneously, the CO_2 molecules adsorbed on the several possible halogen-associated active sites, namely Br1, Br3, and Br5 are activated and reduced by the photogenerated electrons from CB to form CH_4. The electron transfer direction toward CO_2 is evident from the intense electron accumulation, which entails strong CO_2 adsorption and facilitates further activation and subsequent hydrogenation reactions to form CH_4. Based on experimental analysis, the microstructure modulation via incorporation of a secondary halo-

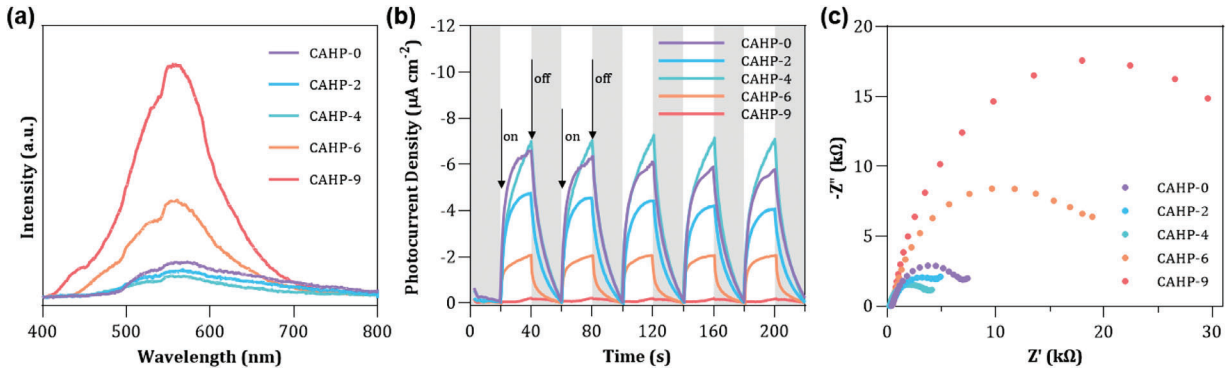

Figure 5. a) Transient photocurrent responses, b) EIS Nyquist plots, and c) Raman-PL spectra of CAHP-*x*.

gen to form mixed halide perovskite induces beneficial charge redistribution to augment surface adsorption and activation of CO_2. The optimum mixture of Br and Cl in the halide perovskite also improves optical properties, promotes charge transfer and separation, annihilates fast charge recombination, allowing more photogenerated electrons and holes to take part in the redox reactions. Overall, these attributes synergistically endow CAHP-4 with an enhanced photocatalytic performance for CO_2 reduction to CH_4.

3. Conclusion

In summary, a series of lead-free $Cs_3Sb_2Cl_xBr_{9-x}$ (CAHP-*x*) photocatalysts was synthesized via a ligand-free and facile antisolvent recrystallization technique at room temperature. By precise tuning of the Cl/Br compositions, the efficiency of charge transfer and separation is exceedingly boosted, suppressing the adverse electron-hole recombination. Eminently, the incorporation of mixed halides elicits charge redistribution across the perovskite framework thereby fostering directional electron delivery as well as strengthening the adsorption and activation abilities of the surface halogen-associated active sites. By virtue of these merits, $Cs_3Sb_2Cl_4Br_5$ (CAHP-4) demonstrated a twofold and fourfold enhancement in photocatalytic CO_2 reduction performance relative to the single halide perovskite counterparts. Through this work, the potential of antimony-based mixed halide perovskite for the photoconversion of CO_2 into CH_4 is explored. We believe that the insights delivered will provide further understanding and prompt future research in the design, development, and utilization of various lead-free perovskite materials with remarkable properties for photocatalysis and other sustainable solar energy applications.

4. Experimental Section

Materials: All chemicals were of analytical grade and used as received without further purification. Caesium chloride (CsCl, 99.9% metal basis), caesium bromide (CsBr, 99.9% metal basis), antimony chloride ($SbCl_3$, 99+ %) and antimony bromide ($SbBr_3$, 99.5% metal basis) were purchased from Alfa Aesar while dichloromethane (CH_2Cl_2, ≥99.5%) was acquired from Macron. Isopropanol (IPA, 99.5%), dimethyl sul-

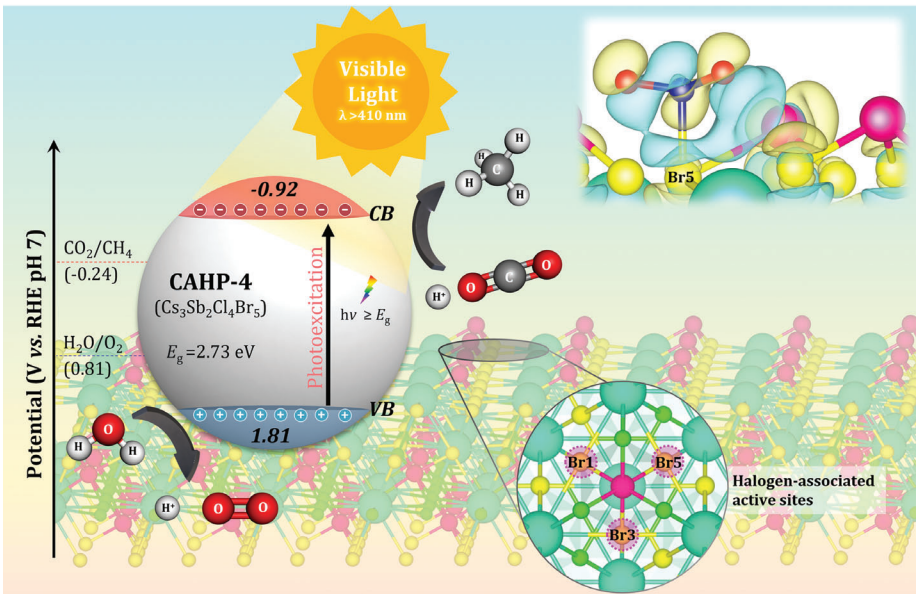

Figure 6. The schematic illustration for the proposed CO_2 photoreduction mechanism over CAHP-4.

foxide (DMSO, 99.5%), and tetrabutylammonium hexafluorophosphate ($TBAPF_6$, 98%, electrochemical grade) were obtained from Sigma Aldrich.

Synthesis of Caesium Antimony Halides $Cs_3Sb_2Cl_xBr_{9-x}$ ($0 \le x \le 9$) perovskites: The $Cs_3Sb_2Cl_xBr_{9-x}$ ($0 \le x \le 9$) samples were synthesized via the antisolvent precipitation method. For the synthesis of $Cs_3Sb_2Br_9$, 0.9 mmol of CsBr and 0.6 mmol of $SbBr_3$ were weighed in a beaker and 10 mL of DMSO solution was added to the Cs and Sb halides. The mixture was stirred and ultrasonicated to completely dissolve CsBr and $SbBr_3$, forming a 30 mM $Cs_3Sb_2Br_9$ precursor solution. The precursor solution was then added by dropwise into a mixture of 20 mL IPA solution with constant vigorous stirring. Hereafter, the suspension was centrifuged at 10 000 rpm for 10 min and subsequently washed two times with IPA. The as-synthesized sample was dried in a vacuum oven at 40 °C overnight. Likewise, the same procedure was applied to synthesize the other $Cs_3Sb_2Cl_xBr_{9-x}$ ($x = 2, 4, 6, 9$) samples, except that the corresponding Cs halides and Sb halides were used to form precursors for injection. The ratios of Cs to Sb halides were kept at 3:2 following Equation (2) below:

$$3CsX + 2SbX_3 \rightarrow Cs_3Sb_2X_9 \quad (2)$$

The caesium antimony halide perovskites $Cs_3Sb_2Cl_xBr_{9-x}$ ($0 \le x \le 9$) were labeled as CAHP-*x*, where $x = 0$, 2, 4, 6, and 9 for $Cs_3Sb_2Br_9$, $Cs_3Sb_2Cl_2Br_7$, $Cs_3Sb_2Cl_4Br_5$, $Cs_3Sb_2Cl_6Br_3$, and $Cs_3Sb_2Cl_9$, respectively.

Sample Characterization: The structural, surface morphology, and elemental composition of the as-synthesized samples were characterized by field emission scanning electron microscopy (FESEM) (Hitachi SU8010) equipped with energy-dispersive X-ray (EDX) (Oxford-Horiba Inca XMax50) and high-resolution transmission electron microscope (HRTEM) (FEI Tecnai G2 20 S-TWIN). Meanwhile, the crystallographic structures of the samples were studied via powder X-ray diffraction (PXRD) measurement on a Bruker D8 Discover X-ray diffractometer with Ni-filtered Cu Kα radiation at a scan rate of 0.02° s^{-1}. To study the chemical states and composition of the constituent elements in the samples, the Phoibos 100 spectrometer (SPECS, Germany) with monochromatic Al-Kα X-ray source was applied for X-ray photoelectron spectroscopy (XPS) measurements. All binding energies were referenced to adventitious carbon signal (C 1s peak) at 284.6 eV prior to deconvolution. Raman spectra were collected by the micro Raman spectrometer Horiba JY LabRAM HR Evolution with an excitation of 785 nm laser light while the room temperature steady-state photoluminescence (PL) spectra were analyzed with the same equipment under PL excitation of a 325 nm He-Cd laser. Furthermore, the DeltaPro Florescence lifetime system (Horiba Scientific) was utilized to record the time-resolved PL (TRPL) spectra at an excitation wavelength of 317 nm. UV–vis diffused reflectance spectra (DRS) were evaluated using a UV–vis spectrophotometer (Agilent, Cary 100) equipped with an integrated sphere and $BaSO_4$ was employed as the reflectance standard. Thermogravimetric analysis (TGA) was investigated under N_2 environment from room temperature to 900 °C using a TGA Q-50-TA instruments.

Photoelectrochemical Measurements: Photoelectrochemical (PEC) measurements were carried out using the Metrohm Autolab electrochemical workstation with a conventional three-electrode PEC setup. The three-electrode cell system is comprised of a Pt rod as the counter electrode, an Ag/AgCl saturated with 3 M KCl as the reference electrode and a working electrode. The working electrodes were assembled by drop casting 2 mL of a photocatalyst suspension onto a fluorine-doped tin oxide (FTO) glass slide with a fixed area of 1 cm × 1 cm. In detail, 6 mg of perovskite sample was dispersed in an isopropanol/Nafion solution (2 mL: 20 µL) to prepare the photocatalyst suspension. With 0.1 M tetrabutylammonium hexafluorophosphate ($TBAPF_6$) in dichloromethane as the electrolyte, the measurements were conducted under light illumination of 150 mW cm^{-2} supplied by a 500 W Xe arc lamp (CHF-XM-500 W). The transient photocurrent responses were recorded at 0 V while electrochemical impedance spectroscopy (EIS) was acquired at an applied bias of −0.6 V in the frequency range of 10^{-2} to 10^5 Hz. Mott Schottky plots were measured in the potential range of 0.2 to 1.0 V versus Ag/AgCl at 1000 Hz.

Evaluation of photocatalytic CO_2 reduction: The photocatalytic CO_2 reduction performances of the photocatalysts were evaluated in a photocatalysis rig under atmospheric pressure and ambient temperature as illustrated in Figure S1, Supporting Information. A 500 W Xe arc lamp (CHF-XM-500 W) was assembled with a UV cut-off filter to simulate visible light ($\lambda > 410$ nm) or without filter for full spectrum irradiation. Prior to the experiments, a thin film of the sample photocatalyst was uniformly coated on glass rods, and the glass rods were loaded into quartz columns positioned 15 cm directly under the light source. The entire reactor setup was enclosed within a customized black box to omit any surrounding light interference. The photoreduction experiments were conducted at ambient conditions (1 atm, 25 °C) in a continuous gas flow reactor. The reactant gas, humidified CO_2 gas generated by bubbling high purity CO_2 gas (99.999%) through a conical flask containing liquid H_2O was introduced into the system via tubing fixed tightly onto both ends of the quartz columns. The gas flow rate was maintained at 50 mL min^{-1} for 1 h to remove excess air and contaminants from the system, as well as to ensure that the photocatalyst surface achieves adsorption-desorption equilibrium. Subsequently the gas flow rate was reduced to 5 mL min^{-1} and maintained for 6 h over the course of the experiment. The gaseous products were quantitatively analyzed at an hourly auto sampling interval by an online gas chromatography (Agilent 8860 GC, He carrier gas) integrated with a flame ionization detector (FID) and thermal conductivity detector (TCD). The resultant product gasses were then quantified using the equation below:

$$CH_4\text{Yield } (\mu\text{mol g}^{-1}) = \frac{\text{Moles of product formed } (\mu\text{mol})}{\text{Mass of photocatalyst used (g)}} \quad (3)$$

Computational Details: The first principle DFT calculations were performed with the Vienna ab initio Simulation Package (VASP).[32] The valence-ionic core interaction was described using the projector-augmented-wave (PAW) method while the exchange and correlation energy was treated in the level of generalized gradient approximation (GGA) using function of Perdew–Burke–Ernzerhof (PBE).[33] A 2 × 2 × 2 unit cell was simulated to model $Cs_3Sb_2Cl_xBr_{9-x}$. The Monkhorst-Pack *k*-point mesh was set at 3 × 3 × 3 for the integration over the Brillouin Zone with a kinetic energy cut-off at 500 eV. The structures were optimized using the conjugate gradient algorithm with the energy convergence criteria of 1.0×10^{-5} eV and force convergence tolerance at 0.01 eV/Å. The details on the construction and relaxation of the structures involved are delineated in Section 4 of the Supplementary Information. After geometry optimization, the projected density of states (DOS) was calculated with the Brillouin Zone sampled using the Monkhorst-Pack *k*-point meshes of 9 × 9 × 9 and the tetrahedron smearing method convergence accuracy of 1.0×10^{-6} eV was applied. CO_2 adsorption studies were executed with Grimmer's DFT-D3 method as an additional Van der Waals (vdW) correction factor to describe the dispersion interactions.[34]

Supporting Information

Supporting Information is available from the Wiley Online Library or from the author.

Acknowledgements

This research project was funded by the Ministry of Higher Education (MOHE) Malaysia under the Fundamental Research Grant Scheme (FRGS) – (Ref No.: FRGS/1/2020/TK0/MUSM/02/1). This work was also supported by High-Performance Computer (HPC) Platform from Monash University Malaysia.

Open access publishing facilitated by Monash University, as part of the Wiley - Monash University agreement via the Council of Australian University Librarians.

Conflict of Interest

The authors declare no conflict of interest.

Data Availability Statement

The data that support the findings of this study are available in the supplementary material of this article.

Keywords

CO_2 reduction, halide tuning, lead-free perovskites, photocatalysis, Sb-based perovskites

Received: March 28, 2023
Revised: May 12, 2023
Published online:

[1] a) W. Wang, S. Wang, X. Ma, J. Gong, *Chem. Soc. Rev.* **2011**, *40*, 3703; b) W. Zhang, A. R. Mohamed, W. J. Ong, *Angew. Chem., Int. Ed.* **2020**, *59*, 22894.
[2] Earth System Research Laboratories Vol. March 12, 2023, Global Monitoring Laboratory **2023**, https://gml.noaa.gov/ccgg/trends/global.html.
[3] C. W. W. Ng, R. Tasnim, J. L. Coo, *Eng. Geol.* **2018**, *242*, 108.
[4] a) M. R. Allen, D. J. Frame, C. Huntingford, C. D. Jones, J. A. Lowe, M. Meinshausen, N. Meinshausen, *Nature* **2009**, *458*, 1163; b) P. Friedlingstein, R. M. Andrew, J. Rogelj, G. P. Peters, J. G. Canadell, R. Knutti, G. Luderer, M. R. Raupach, M. Schaeffer, D. P. van Vuuren, C. L.e Quéré, *Nat. Geosci.* **2014**, *7*, 709; c) M. S. Dresselhaus, I. L. Thomas, *Nature* **2001**, *414*, 332; d) J. Qiao, Y. Liu, F. Hong, J. Zhang, *Chem. Soc. Rev.* **2014**, *43*, 631.
[5] R. Meys, A. Kätelhön, M. Bachmann, B. Winter, C. Zibunas, S. Suh, A. Bardow, *Science* **2021**, *374*, 71.
[6] X. Y. Kong, T. Tong, B. J. Ng, J. Low, T. H. Zeng, A. R. Mohamed, J. Yu, S. P. Chai, *ACS Appl. Mater. Interfaces* **2020**, *12*, 26991.
[7] G. H. Han, J. Bang, G. Park, S. Choe, Y. J. Jang, H. W. Jang, S. Y. Kim, S. H. Ahn, *Small* **2023**, *19*, 2205765.
[8] a) Z. R. Miao, Q. L. Wang, Y. F. Zhang, L. P. Meng, X. X. Wang, *Appl. Catal. B* **2022**, *301*, 120802; b) L. B. Wang, B. Cheng, L. Y. Zhang, J. G. Yu, *Small* **2021**, *17*, 2103447; c) J. Zhou, J. Li, L. Kan, L. Zhang, Q. Huang, Y. Yan, Y. F. Chen, J. Liu, S. L. Li, Y. Q. Lan, *Nat. Commun.* **2022**, *13*, 4681; d) J. Li, H. L. Huang, W. J. Xue, K. Sun, X. H. Song, C. R. Wu, L. Nie, Y. Li, C. Y. Liu, Y. Pan, H. L. Jiang, D. H. Mei, C. L. Zhong, *Nat. Catal.* **2021**, *4*, 719.
[9] a) S. Shyamal, N. Pradhan, *J. Phys. Chem. Lett.* **2020**, *11*, 6921; b) M. A. Raza, F. Li, M. Que, L. Zhu, X. Chen, *Mater. Adv.* **2021**, *2*, 7187; c) Z. C. Kong, J. F. Liao, Y. J. Dong, Y. F. Xu, H. Y. Chen, D. B. Kuang, C. Y. Su, *ACS Energy Lett.* **2018**, *3*, 2656.
[10] a) J. N. Huang, Y. J. Dong, H. B. Zhao, H. Y. Chen, D. B. Kuang, C. Y. Su, *J. Mater. Chem. A* **2022**, *10*, 25212; b) R. Das, A. Patra, S. K. Dutta, S. Shyamal, N. Pradhan, *J. Am. Chem. Soc.* **2022**, *144*, 18629; c) Z. Zhang, L. Li, Y. Jiang, J. Xu, *Inorg. Chem.* **2022**, *61*, 3351.
[11] C. B. Hiragond, N. S. Powar, S. I. In, *Nanomaterials* **2020**, *10*, 2569.
[12] Q. Fan, G. V. Biesold-McGee, J. Ma, Q. Xu, S. Pan, J. Peng, Z. Lin, *Angew. Chem., Int. Ed.* **2020**, *59*, 1030.
[13] a) S. K. Shil, F. Wang, K. O. Egbo, Z. X. Lai, Y. Wang, Y. P. Wang, D. X. Zhao, S. W. Tsang, J. C. Ho, K. M. Yu, *ACS Appl. Mater. Interfaces* **2021**, *13*, 35930; b) S. Y. Kim, D. A. Park, N. G. Park, *ACS Appl. Electron. Mater.* **2022**, *4*, 2388; c) F. Cao, Z. Q. Li, X. Y. Liu, Z. F. Shi, X. S. Fang, *Adv. Funct. Mater.* **2022**, *32*, 2206151.
[14] a) Y. Wang, Q. Zhou, Y. Zhu, D. Xu, *Appl. Catal., B* **2021**, *294*, 120236; b) Y. Hai, W. Huang, Z. Li, D. Wu, Q. Huang, X. Tang, *ACS Appl. Energy Mater.* **2021**, *4*, 5913; c) C. Lu, D. S. Itanze, A. G. Aragon, X. Ma, H. Li, K. B. Ucer, C. Hewitt, D. L. Carroll, R. T. Williams, Y. Qiu, S. M. Geyer, *Nanoscale* **2020**, *12*, 2987.
[15] D. Wu, B. Huo, Y. Huang, X. Zhao, J. Yang, K. Hu, X. Mao, P. He, Q. Huang, X. Tang, *Small* **2022**, *18*, 2106001.
[16] S. Chen, H. Yin, P. Liu, Y. Wang, H. Zhao, *Adv. Mater.* **2023**, *35*, 2203836.
[17] a) X. Wang, N. Ali, G. Bi, Y. Wang, Q. Shen, A. Rahimi-Iman, H. Wu, *Inorg. Chem.* **2020**, *59*, 15289; b) S. Paul, S. Sain, T. Kamilya, A. Dalui, P. K. Sarkar, S. Acharya, *Mater. Today Chem.* **2022**, *23*, 100641.
[18] a) Z. Y. Zhao, Q. L. Liu, W. W. Dai, *Sci. Rep.* **2016**, *6*, 31449; b) E. Keller, V. Krämer, **2005**, *60*, 1255.
[19] a) M. Shi, G. Li, W. Tian, S. Jin, X. Tao, Y. Jiang, E. A. Pidko, R. Li, C. Li, *Adv. Mater.* **2020**, *32*, 2002137; b) K. K. Bass, L. Estergreen, C. N. Savory, J. Buckeridge, D. O. Scanlon, P. I. Djurovich, S. E. Bradforth, M. E. Thompson, B. C. Melot, *Inorg. Chem.* **2017**, *56*, 42.
[20] a) M. Shi, H. Zhou, W. Tian, B. Yang, S. Yang, K. Han, R. Li, C. Li, *Cell Rep. Phys. Sci.* **2021**, *2*, 100656; b) W. K. Chong, B. J. Ng, X. Y. Kong, L. L. Tan, L. K. Putri, S. P. Chai, *Appl. Catal., B* **2023**, *325*, 122372.
[21] A. Pradhan, M. K. Jena, S. L. Samal, *ACS Appl. Energy Mater.* **2022**, *5*, 6952.
[22] A. Pradhan, S. C. Sahoo, A. K. Sahu, S. L. Samal, *Cryst. Growth Des.* **2020**, *20*, 3386.
[23] a) D. Wu, X. Zhao, Y. Huang, J. Lai, H. Li, J. Yang, C. Tian, P. He, Q. Huang, X. Tang, *Chem. Mater.* **2021**, *33*, 4971; b) D. Wu, X. Zhao, Y. Huang, J. Lai, J. Yang, C. Tian, P. He, Q. Huang, X. Tang, *J. Phys. Chem. C* **2021**, *125*, 18328; c) Q. Huang, C. Tian, J. Lai, F. Qi, N. Zhang, J. Liu, Z. Liang, D. Wu, X. Tang, *Inorg. Chem.* **2022**, *61*, 14447.
[24] a) P. Liu, Y. Liu, S. Zhang, J. Li, C. Wang, C. Zhao, P. Nie, Y. Dong, X. Zhang, S. Zhao, G. Wei, *Adv. Opt. Mater.* **2020**, *8*, 2001072; b) Y. L. Liu, C. L. Yang, M. S. Wang, X. G. Ma, Y. G. Yi, *J. Mater. Sci.* **2019**, *54*, 4732.
[25] J. P. Perdew, *Int. J. Quantum Chem.* **1985**, *28*, 497.
[26] A. Álvarez, M. Borges, J. J. Corral-Pérez, J. G. Olcina, L. Hu, D. Cornu, R. Huang, D. Stoian, A. Urakawa, *ChemPhysChem* **2017**, *18*, 3135.
[27] G. Chen, P. Wang, Y. Wu, Q. Zhang, Q. Wu, Z. Wang, Z. Zheng, Y. Liu, Y. Dai, B. Huang, *Adv. Mater.* **2020**, *32*, 2001344.
[28] B. J. Ng, W. K. Chong, L. K. Putri, X. Y. Kong, J. Low, H. W. Lee, L. L. Tan, W. S. Chang, S. P. Chai, *J. Mater. Chem. A* **2023**.
[29] a) Y. Wu, P. Wang, Z. Guan, J. Liu, Z. Wang, Z. Zheng, S. Jin, Y. Dai, M. H. Whangbo, B. Huang, *ACS Catal.* **2018**, *8*, 10349; b) Y. Tang, C. H. Mak, C. Wang, Y. Fu, F. F. Li, G. Jia, C. W. Hsieh, H. H. Shen, J. C. Colmenares, H. Song, M. Yuan, Y. Chen, H. Y. Hsu, *Small Methods* **2022**, *6*, 2200326; c) Y. Tang, C. H. Mak, J. Zhang, G. Jia, K. C. Cheng, H. Song, M. Yuan, S. Zhao, J. J. Kai, J. C. Colmenares, H. Y. Hsu, *Adv. Mater.* **2023**, *35*, 2207835.
[30] J. Lee, S. H. W. Kok, B. J. Ng, X. Y. Kong, L. K. Putri, S. P. Chai, L. L. Tan, *J. Environ. Chem. Eng.* **2023**, *11*, 109511.
[31] J. Sheng, Y. He, J. Li, C. Yuan, H. Huang, S. Wang, Y. Sun, Z. Wang, F. Dong, *ACS Nano* **2020**, *14*, 13103.
[32] a) G. Kresse, J. Furthmüller, *Phys. Rev. B* **1996**, *54*, 11169; b) G. Kresse, J. Hafner, *Phys. Rev. B* **1993**, *47*, 558.
[33] a) P. Li, Y. Lin, M. Ma, M. Zhang, J. Li, Z. Wang, V. Maheskumar, Z. Y. Jiang, R. Zhang, *ACS Appl. Energy Mater.* **2022**, *5*, 1942; b) J. P. Perdew, K. Burke, M. Ernzerhof, *Phys. Rev. Lett.* **1996**, *77*, 3865.
[34] a) J. M. Meng, Z. X. Yang, S. B. Patil, J. C. Lin, C. H. Yeh, Y. C. Chen, C. W. Pao, J. L. Chen, W. Y. Chen, C. W. Lu, T. R. Kuo, D. Y. Wang, *J. Phys. Chem. Lett.* **2021**, *12*, 8763; b) Q. M. Sun, J. J. Xu, F. F. Tao, W. Ye, C. Zhou, J. H. He, J. M. Lu, *Angew. Chem., Int. Ed.* **2022**, *61*, e202200872; c) S. Grimme, S. Ehrlich, L. Goerigk, *J. Comput. Chem.* **2011**, *32*, 1456.